Observer-Based Adaptive Robust Control of Friction Stir Welding Axial Force

Tyler A. Davis, Yung C. Shin, and Bin Yao, *Member, IEEE*

***Abstract*—Friction stir welding (FSW) is a relatively new and promising joining process that is the subject of much current research. When welding with constant parameters, the axial force can vary significantly due to changes in workpiece temperature and other process variations. These variations produce welds with inconsistent microstructure and tensile strength. Control of the axial weld force is desirable to improve the weld quality. In this paper, an observer-based adaptive robust control (ARC) approach for the axial force of FSW is presented to overcome process disturbances and model errors stemming from the simplistic dynamic models suitable for control. Some correlation is shown between spindle power and axial force, allowing readily available power measurements to be used for feedback. A model of the axial force is developed as a combination of a nonlinear static gain and linear dynamics. An axial force controller is constructed using the ARC approach and estimated state feedback from the adaptive divided difference filter (ADDF). Verification experiments are conducted on a vertical milling machine configured for FSW using an open architecture controller. The combined ARC/ADDF technique is shown to dramatically reduce axial force variations in the presence of significant process disturbances.**

***Index Terms*—Force control, friction stir welding (FSW), nonlinear systems, observers.**

I. Introduction

FRICTION stir welding (FSW) is a promising new joining process that is currently under heavy research. The FSW process is typically used for aluminum alloys, but can be used for other materials, including steel, titanium, and plastic. The process uses a nonconsumable rotating tool consisting of a pin extending below a shoulder that, in a butt-weld configuration, is forced completely into the adjacent mating edges of two plates. This process is illustrated in Fig. 1. Heat input from the material plastic deformation and friction of the tool softens the material. Combining the heat input and forging action of the tool shoulder with the stirring action of the tool induces a plastic flow in the material, forming a solid-state weld [1].

FSW control applications are subject to significant process variations. For example, variations in workpiece geometry can alter the heat transfer when welding. Changes in heat transfer, and thus local workpiece temperature, lead to changes in the weld force. Plunge depth may change during welding due to inconsistent surface flatness thus affecting welding force.

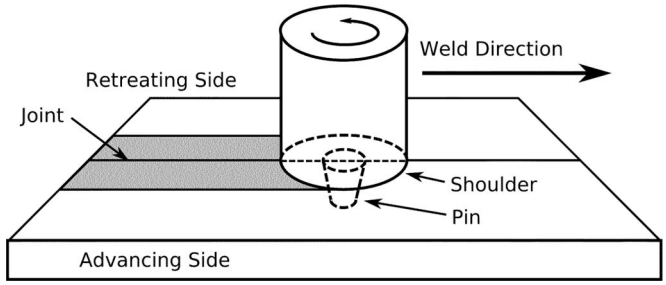

Fig. 1. FSW arrangement.

Effects such as these cannot be captured in a dynamic model, and therefore must be addressed by the controller.

A number of research works on axial force control are available in the literature. In [2], axial force control is implemented using position control of a robot arm to regulate plunge depth in order to maintain a constant axial welding force. While effective, this approach also produces an uneven surface finish. Since the majority of the force increase resulting from increased plunge depth is transitory, this approach can lead to instability in the form of constantly increasing plunge depth. For these reasons, plunge depth is not a suitable control variable for force control.

Zhao *et al.* [3] and Oakes and Landers [4] also use the plunge depth to control force with a discrete controller designed by pole placement. This design approach is viable, but lacks any mechanism for handling uncertainties. Force sensing is accomplished by mounting six-axis force sensors to the welding head. Such sensors can be prohibitively expensive or impractical when retrofitting industrial equipment. Soron and Kalaykov [5] show that industrial robots with existing force controllers can be used for FSW force control, but again use plunge depth as the control variable.

The main process variables governing FSW are spindle speed, traverse rate, and plunge depth. Since traverse speeds are small when compared with spindle speeds, the relative velocity between the tool and workpiece—and thus the heat generation rate—is essentially governed by the spindle speed [6], [7]. Increasing the traverse speed leads to a decrease in the average heat input and a slightly lower material temperature, which in turn increases the force exerted on the tool. Decreasing the traverse speed has the opposite effect. Higher temperatures increase the size of the thermally affected zone, but also decrease the size of the deformation region by improving the material flow around the pin. Utilizing traverse speed as the control variable therefore has the advantage of producing a weld with more consistent

Manuscript received March 19, 2010; revised June 30, 2010; accepted August 16, 2010. Date of publication October 7, 2010; date of current version September 7, 2011. Recommended by Technical Editor J. M. Berg.

The authors are with the School of Mechanical Engineering, Purdue University, West Lafayette, IN 47907 USA (e-mail: davis152@purdue.edu; shin@purdue.edu; byao@purdue.edu).

Digital Object Identifier 10.1109/TMECH.2010.2071417

microstructure qualities while maintaining a constant plunge depth to produce an even surface.

The performance of common linear control techniques such as PID or various state space methods can suffer from the presence of model uncertainties or disturbances. When applied to nonlinear systems, the ignored nonlinearities may be large enough to destabilize linear controllers. Adaptive controllers (AC) such as those introduced in [8] and [9] produce excellent control results for nonlinear systems in response to linear plant parameter variation. However, nonlinear uncertainties and disturbances can introduce steady-state tracking error, diminish the transient performance, and may cause the control system to lose stability. Robust controllers (RC) [10], [11] or the sliding mode controller (SMC) [12] can guarantee the transient performance as well as the steady-state error in the presence of uncertainties and disturbances, but these designs suffer from the matching condition problem and utilize high or switched gains that are unrealizable or introduce control input chattering.

The adaptive robust control (ARC) discussed in [13] combines the AC and RC techniques by taking advantage of reasonably available system information such as parameter variation bounds to utilize the strengths of each method while eliminating their shortcomings. Using ARC in a backstepping framework [14]–[16] avoids the matching condition problem and makes the ARC technique systematically applicable to systems in the semistrict feedback form. The backstepping approach requires that all system states be available for feedback, which is impossible for many systems. Therefore, an observer is required to estimate the unmeasured states.

Nonlinear observers are typically constructed using the system model in combination with existing nonlinear control techniques such as sliding mode [17] or unique Lyapunov-based applications [18], [19]. These methods are difficult to apply in a systematic manner, so efforts have been made to develop nonlinear extensions of systematic linear techniques. Most common is the extended Kalman filter (EKF) [20]. This approach is based on a first-order linearization of the nonlinear system that frequently introduces enough error to cause significant estimate error or even stability problems. The inadequacies of the EKF have been largely resolved by a number of improved methods such as the unscented Kalman filter (UKF) [21] and the divided difference filter (DDF) [22]. However, even the improved methods can diverge in the presence of model error. To address the issue of estimate divergence resulting from model error an adaptive divided difference filter (ADDF) has been developed in [23].

By using ARC in a backstepping framework supported by ADDF state estimates, a robust and adaptive nonlinear observer-based control scheme is achieved. This scheme can be systematically applied to a large set of nonlinear control problems, including many that are encountered in manufacturing. In this paper, the combined ARC/ADDF approach is used to control the axial force of FSW. A spindle power-based feedback signal is used to eliminate the need for expensive force sensors. The traverse rate is used as the plant input to improve weld quality and surface finish. Experimental implementation of the approach is provided.

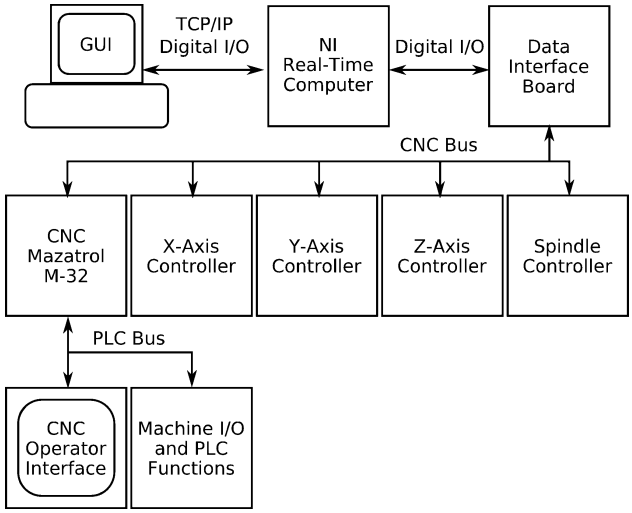

Fig. 2. Mazak OAC layout.

TABLE I
MAZAK COMMUNICATION SPECIFICATIONS

	Sample Time (ms)	Resolution
x-axis	3.55	0.0001 mm
y-axis	3.55	0.0001 mm
z-axis	3.55	0.0005 mm
spindle (command)	56.8	0.682 RPM
spindle (feedback)	56.8	1 RPM

II. EXPERIMENTAL SETUP

The FSW experimental setup consists of a Mazak VQC-15/40 vertical machining center configured to perform butt welds. Since this is a conventional computer numerical controlled (CNC) machining center, a small welding tool must be used to keep the welding forces within ranges that are safe for the mill. The Mazak can be controlled using an open architecture controller (OAC) developed in [24], which has been upgraded with a National Instruments real-time operating system computer [25]. The OAC can send axis position and spindle velocity commands to the Mazak, as well as receive feedback signals reporting the true position and spindle velocity. The axis and spindle commands override those sent by the built-in Mazatrol M-32 controller while leaving the programmable logic controller (PLC) functions such as overtravel switches and emergency stops intact.

The OAC is implemented using a National Instruments (NI) PXI-8176 computer with the LabView real-time operating system to ensure deterministic calculation of axes commands. The computer uses digital I/O cards to communicate with the in-house built data interface board that in turn communicates with the axes drive data bus. A graphical user interface (GUI) is implemented on a remote desktop computer. Communication between the GUI and the real-time operating system is accomplished using a combination of TCP/IP and high-speed digital I/O protocols. This arrangement is illustrated in Fig. 2. The communication sample time and resolution for each axis of the Mazak is listed in Table I.

The FSW tool has a shoulder diameter of 5 mm with a tapered pin that is threaded and has three flats. The pin is 2.5 mm long with an upper diameter of 3.0 mm and a lower diameter of 2.0 mm. The workpieces are $76 \times 101 \times 6.35$ mm plates of 7075 aluminum. The plates are mounted to a 25.4-mm-thick steel backing plate, using two bolts and two clamps. This backing plate is used to prevent flexing of the workpiece by providing support against the axial force of the welding. The backing plate can be mounted to a dynamometer to allow force measurements, or directly to the work table.

The welding forces are measured using a three axes Kistler 9257B dynamometer with a Kistler 5004 dual mode amplifier. The dynamometer output is then sampled by the NI computer. The spindle motor power is simultaneously measured with a Load Controls, Inc., PH-3 A power cell that is also sampled by the NI computer, and is used as the process feedback signal. Direct force measurements from the dynamometer are used only for experimental verification.

III. Force Measurement

As an alternative to expensive or impractical force sensors, the spindle motor power is considered as a force feedback signal. Spindle motor power sensors are much less expensive than force sensors and are already present on most machine tools. The use of spindle motor power as a force feedback signal is described below.

A. Force Calculation From Power

In [26], the authors calculate tool P_t (W), or heat input per unit time q_0, as

$$q_0 = P_t = SM = \frac{2}{3}\mu_e \pi S p R^3 \tag{1}$$

where S (r/s) is the spindle speed, M (Nm) is the torque, μ_e is an effective friction coefficient that lumps the effects of spindle motor efficiency, tool pin profile, and workpiece shearing, p (Pa) is the pressure on the plate, and R (m) is the radius of the tool shoulder. Since the axial force is $F_z = \pi p R^2$ (N), one can obtain

$$P_t = \frac{2}{3}\mu_e S F_z R. \tag{2}$$

The tool power can be related to the measured spindle power P_m (W) by subtracting the power required to idle the tool P_i (W) at a given spindle speed: $P_t = P_m - P_i$. Combining this with (2) and solving for F_z allows the axial force to be calculated from the measured power as

$$F_z = 90\frac{(P_m - P_i)}{(2\pi\mu_e \omega R)} \tag{3}$$

where $\omega = (60/2\pi S)$ is the spindle speed in RPM.

B. Spindle Idle Power Identification

The idle power was identified by measuring the spindle power at various speeds in the expected FSW operating range of 1000–3000 RPM (CCW) while idling the spindle. The power was measured both with and without the tool in the spindle, and linear trend lines were fit to both sets of data. The data show a good fit with $R^2 = 0.999$ in both cases. The relationship including the tool was selected, i.e.,

$$P_i = a_i \omega + b_i = 0.13\omega + 24.3 \tag{4}$$

where a_i and b_i are linear fit coefficients. Combining (4) with (3) yields the final axial force equation

$$F_z = \frac{90}{(2\pi\mu_e R)}\left(\frac{P_m - b_i}{\omega - a_i}\right). \tag{5}$$

TABLE II
Friction Coefficient Experiment Conditions

Experiment #		Plunge Depth (mm)	Feed Rate (mm/min)
2500 RPM	2000 RPM		
1	10	0.02	120
2	11	0.11	120
3	12	0.20	120
4	13	0.02	180
5	14	0.11	180
6	15	0.20	180
7	16	0.02	240
8	17	0.11	240
9	18	0.20	240

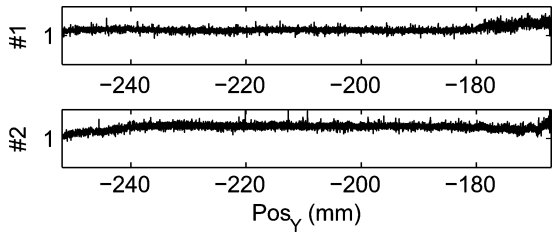

Fig. 3. Calculated μ_e for experiments 1–2 (typical of remaining experiments).

C. Effective Friction Coefficient Identification

To identify μ_e welding experiments were performed across a range of values for spindle speed, plunge depth, and feed rate. The selected experimental conditions are listed in Table II. Measurements of the weld forces and spindle power were taken during welding. Each welding process consists of three stages: plunging into the workpiece at a rate of 12 mm/min, preheat welding at a rate of 40 mm/min for 5 mm, and finally, welding at full speed for 85 mm. At the end of the weld, the tool is immediately withdrawn from the workpiece. All welding operations are performed on the face of a single workpiece, i.e., bead-on-plate.

The experimental data are used to identify the effective friction coefficient by solving for μ_e in (5). The friction coefficient value fluctuates during the tool plunge and preheating stages of the welding process, but becomes nearly constant during the full speed portion of the weld. This trend is shown in Fig. 3 for the first two experiments. The average experimental friction coefficient is 1.12 with a standard deviation of 0.09.

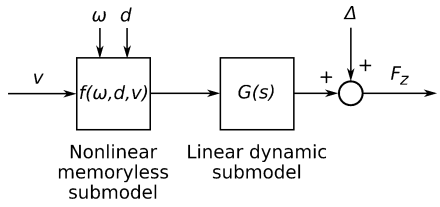

Fig. 4. Proposed model structure.

IV. Axial Force Dynamics

The dynamic model for axial force of FSW F_z (N) is constructed as the combination of a static nonlinear input gain portion and a unity gain linear dynamic portion in an approach based on the Hammerstein model [27], as shown in Fig. 4. The input velocity v, spindle speed ω, and plunge depth d are mapped through the nonlinear input gain $f(\omega, d, v)$. The linear dynamic submodel represents the dynamic behavior of the average axial force F_z. An output disturbance Δ is also considered.

The dynamic model is fit to the step responses taken from experiments 13 and 14 (described in Table II) across the transition from slow speed preheating to normal welding regions. This corresponds to a traverse velocity step change from 40 to 180 mm/min. The experimental axial force data contain noise at 33.3 Hz (2000 RPM) from the spindle rotation. A Fourier analysis of the spindle power measurement did not contain any significant component at 33.3 Hz, thus it is believed that this force fluctuation is due to the run out of the tool. This noise was filtered out to aid model identification using a fourth-order low-pass Butterworth filter with a cutoff frequency of 15 Hz.

The filtered data are next offset and scaled to yield a unity gain step response. The dynamic response of the offset and normalized data is represented by the transfer function

$$\frac{(F_z - F_{z,0})}{(F_{z,ss} - F_{z,0})} = G(s) \tag{6}$$

where $F_{z,0}, F_{z,ss}$ are the initial and steady-state axial force values, respectively. A continuous unity gain model was fit to the offset and normalized data using the MATLAB system identification toolbox. The resulting model is

$$G(s) = \frac{614.6}{s^2 + 54.57s + 614.6}. \tag{7}$$

The full-scale signal can be reconstructed by rearranging (7) as

$$F_z = G(s)(F_{z,ss} - F_{z,0}) + F_{z,0}. \tag{8}$$

The full-scale simulated dynamics are compared with the unaltered experimental data in Fig. 5.

The input parameters will be used to model the steady-state axial force using the form

$$F_{z,ss} = f(\omega, d, v) = K\omega^{\alpha} d^{\beta} v^{\gamma} \tag{9}$$

similar to that used in [28]. K, α, β, γ are coefficients that must be determined. Force data collected from the friction coefficient experiments show that a steady-state axial force is rarely achieved during the full-speed welding portion. To fit a model such as (9) an effective average force for each experiment was determined by taking the average of the axial force over the last half of the full-speed portion of each weld. This region was selected to capture the typical amount of variation while excluding any start-up transients. One additional data point was taken from the "slow" portion of exp. #13 just prior to the step change to normal traverse speed. It is referred to below as exp. #0. This data point was added to allow the static model to include the parameter range used in the dynamic step response analysis. The force variation during the normal speed portion of the process is significant, as shown in Fig. 6. Variations of over 500 N are common, and the nature of the variation is not repeatable. The axial force tends to increase with increasing traverse rate and decreasing spindle speed. The effect of plunge depth is less consistent—sometimes increasing the force and sometimes decreasing it.

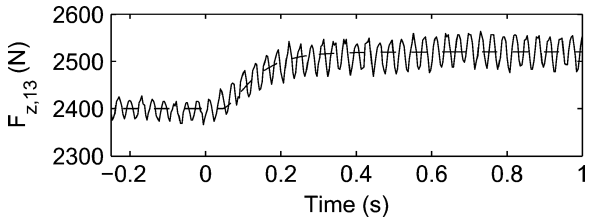

Fig 5. Full-scale simulated dynamic response (dashed) compared with experimental axial force response to traverse velocity step change from 40 to 180 mm/min from experiment #13 (solid).

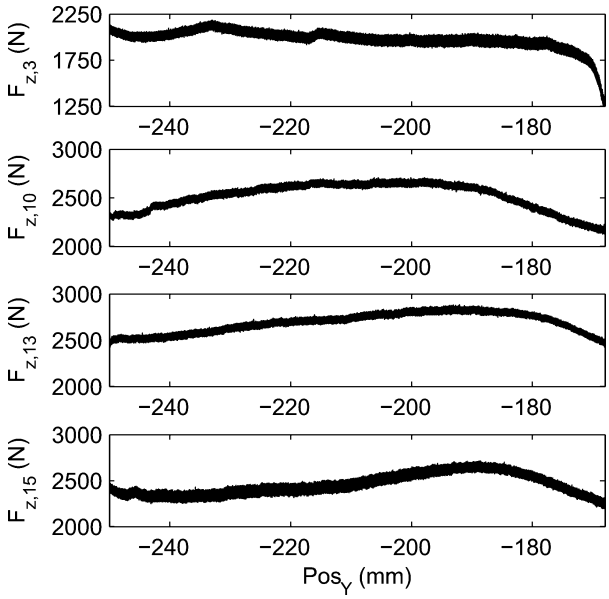

Fig. 6. Typical axial force variation during the constant parameter portion of a stir weld.

The model coefficients were fit using the least squares approach after setting $K = e^{\kappa}$ and taking the natural log of (9), i.e.,

$$\begin{aligned} \ln(F_{z,ss}) &= \ln\left(e^{\kappa}\omega^{\alpha} d^{\beta} v^{\gamma}\right) \\ &= \kappa \cdot 1 + \alpha \ln(\omega) + \beta \ln(d) + \gamma \ln(v) \\ &= 12.92 - 0.7817 \ln(\omega) - 0.0308 \ln(d) \\ &\quad + 0.1623 \ln(v). \end{aligned} \tag{10}$$

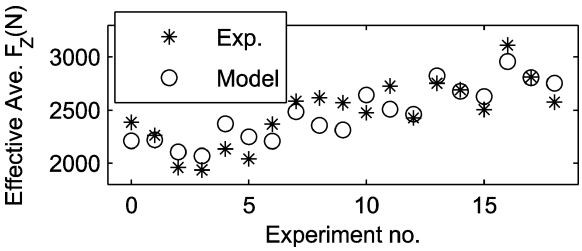

Fig. 7. Experimental versus modeled forces.

After fitting, the R^2 coefficient is .702 and the average absolute error is 141 N. The model predictions are compared with the experimental data in Fig. 7. The model captures the general trend of the data, but does not accurately predict each point. This is as good as can be expected since the large axial force variations in the identification experiments prevent the true steady state force values from being observed. Adaptive control will be required for good system performance with such large model error.

One can obtain from equations (8) and (9)

$$F_z = G(s)\left(f(\omega,d,v) - f(\omega,d,v_0)\right) + f(\omega,d,v_0). \quad (11)$$

Defining an offset regime "$*$" for control design where $F_z^* = F_z - f(\omega,d,v_0)$ and $f^*(\omega,d,v) = f(\omega,d,v) - f(\omega,d,v_0)$ and substituting them into (11) yields the nominal offset dynamics

$$\begin{aligned} F_z^* &= G(s) f^*(\omega,d,v) \\ &= \frac{614.6}{s^2+54.57s+614.6} e^{12.92}\omega^{-0.7817} d^{-0.0308} v^{0.1623}. \end{aligned} \quad (12)$$

For a given set of constant parameter values ω and d the simplified notation $f^*_{\omega,d}(v)$ is used for the nonlinear input gain. After including the output disturbance the dynamic model is represented in the state-space form as

$$\begin{aligned} \dot{\zeta} &= A\zeta + B f^*_{\omega,d}(v) \\ F_z^* &= C\zeta + \Delta \end{aligned} \quad (13)$$

where ζ is the state vector and

$$A = \begin{bmatrix} 0 & 1 \\ -614.6 & -54.57 \end{bmatrix} B = \begin{bmatrix} 0 \\ 614.6 \end{bmatrix} C = \begin{bmatrix} 1 & 0 \end{bmatrix}.$$

The modeled magnitude shows significant error during the weld due to the large disturbances, but is at least in the correct range of the weld force when comparing the modeled step response with the full duration of the normal weld. Variations in the substrate surface cause the actual plunge depth to change during the welding process, which leads to uncertainty in the value of $f^*_{\omega,d}$. This uncertainty is represented by introducing a bounded unknown parameter θ_1 such that $f^*_{\omega,d} = \theta_1 \hat{f}^*_{\omega,d}$. To accommodate control design the system input can be linearized with the substitution $u = \hat{f}^*_{\omega,d}(v)$. After determining the control effort u the commanded velocity is then calculated from $v = \hat{f}^{*,-1}_{\omega,d}(u)$. The output disturbance is defined as $\Delta = \theta_2 + \tilde{\Delta}$ where θ_2 is a bounded unknown parameter representing the slowly varying component of the disturbance, and $\tilde{\Delta}$ represents the high frequency noise. The linearized model dynamics are now represented in terms of the unknown parameters θ_1, θ_2 as

$$\begin{aligned} \dot{\zeta} &= A\zeta + B\theta_1 u \\ F_z^* &= C\zeta + \theta_2 + \tilde{\Delta}. \end{aligned} \quad (14)$$

Define the parameter estimates $\hat{\theta}_i = \theta_i - \tilde{\theta}_i$, where $\tilde{\theta}_i$ is the estimate error. Assuming that the bounds $\theta_{i,\min}$ and $\theta_{i,\max}$ of θ_i are known, the following discontinuous projection adaption law will be used

$$\dot{\hat{\theta}}_i = \mathrm{Proj}_{\hat{\theta}_i}(\gamma_i \tau_i) \quad (15)$$

where $\gamma_i > 0$ is the adaptation gain and τ_i is an adaptation function that will be determined later. The projection mapping is defined in [15] as

$$\mathrm{Proj}_{\hat{\theta}_i}(\bullet_i) = \begin{cases} 0, & \text{if } \hat{\theta}_i = \theta_{i,\max} \text{ and } \bullet_i > 0 \\ 0, & \text{if } \hat{\theta}_i = \theta_{i,\min} \text{ and } \bullet_i < 0 \\ \bullet_i, & \text{otherwise.} \end{cases} \quad (16)$$

V. Control Design

The ARC method is applied to the system in a backstepping framework to accommodate the unmatched disturbances in the system. The first state can be calculated from the output measurement, but the second state must be estimated. Observer design for the second state will be discussed in the following section. The first error term is defined as $z_1 = F_z^* - F^*_{z,d}$ and has the derivative $\dot{z}_1 = \zeta_2 + \dot{\tilde{\Delta}} - \dot{F}^*_{z,d}$. The first virtual control law can then be chosen as

$$\zeta_{2,d} = -k_1 z_1 + \dot{F}^*_{z,d} + \alpha_{1s} \quad (17)$$

where $k_1 > 0$ is a control gain and α_{1s} is a robust control term which is designed later. The second error term is then $z_2 = \zeta_2 - \zeta_{2,d}$. The dynamics of the first error term are considered with the Lyapunov function $V_1 = {}^1\!/_2 z_1^2$, which has the derivative

$$\begin{aligned} \dot{V}_1 &= z_1 \dot{z}_1 \\ &= z_1(\zeta_2 + \dot{\tilde{\Delta}} - \dot{F}^*_{z,d}) \\ &= z_1(z_2 + \zeta_{2,d} + \dot{\tilde{\Delta}} - \dot{F}^*_{z,d}) \\ &= z_1(z_2 - k_1 z_1 + \dot{F}^*_{z,d} + \alpha_{1s} + \dot{\tilde{\Delta}} - \dot{F}^*_{z,d}) \\ &= -k_1 z_1^2 + z_1(\alpha_{1s} + \dot{\tilde{\Delta}}) + z_1 z_2. \end{aligned} \quad (18)$$

A Lyapunov function considering both error terms is $V_2 = {}^1\!/_2 z_1^2 + {}^1\!/_2 z_2^2$, which has the derivative

$$\begin{aligned} \dot{V}_2 &= z_1 \dot{z}_1 + z_2 \dot{z}_2 \\ &= -k_1 z_1^2 + z_1(\alpha_{1s} + \dot{\tilde{\Delta}}) + z_2(z_1 + \dot{z}_2) \end{aligned} \quad (19)$$

where

$$\dot{z}_2 = -614.6\zeta_1 - 54.57\zeta_2 + 614.6\theta_1 u + k_1 \dot{z}_1 - \ddot{F}^*_{z,d} + \dot{\alpha}_{1s}. \quad (20)$$

Substituting $\zeta_1 = F_z^* - \theta_2 - \tilde{\Delta}$ from the output equation and $\dot{z}_1$ from earlier into (20) yields

$$\dot{z}_2 = -614.6(F_z^* - \theta_2 - \tilde{\Delta}) - 54.57\zeta_2 + 614.6\theta_1 u$$

$$+k_1\zeta_2 + k_1\dot{\tilde{\Delta}} - k_1\dot{F}^*_{z,d} - \ddot{F}^*_{z,d} + \dot{\alpha}_{1s}. \quad (21)$$

The control law $u = u_a + u_s$, where u_a is a model compensation term and u_s is a robust term, can now be constructed. The control law must use $\hat{\theta}_1, \hat{\theta}_2, \hat{\zeta}_2$ since the actual values are not available. This lead to a final control law of

$$u_a = \frac{1}{614.6\hat{\theta}_1}\begin{pmatrix} 614.6(F^*_z - \hat{\theta}_2) + 54.57\hat{\zeta}_2 - k_1(\hat{\zeta}_2 - \dot{F}^*_{z,d}) \\ + \ddot{F}^*_{z,d} - \dot{\alpha}_{1s} \end{pmatrix}$$

$$u_s = \frac{1}{614.6\hat{\theta}_1}(-k_2 z_2 - z_1 + \alpha_{2s}) \quad (22)$$

where $k_2 > 0$ is a control gain and α_{2s} is a robust term designed later. Substituting (22) into (21) produces the Lyapunov function dynamics

$$\begin{aligned}\dot{V}_2 = {} & -k_1 z_1^2 + z_1(\alpha_{1s} + \dot{\tilde{\Delta}}) - k_2 z_2^2 \\ & + z_2(-614.6(\tilde{\theta}_1 u + \tilde{\theta}_2 - \tilde{\Delta} - k_1\tilde{\zeta}_2 + k_1\dot{\tilde{\Delta}}) \\ & + 54.57\tilde{\zeta}_2 + \alpha_{2s}) \end{aligned} \quad (23)$$

which are stable if

$$\begin{aligned} & z_1(\alpha_{1s} + \dot{\tilde{\Delta}}) \le \varepsilon_1 \\ & z_2(-614.6(\tilde{\theta}_1 u + \tilde{\theta}_2 - \tilde{\Delta} - k_1\tilde{\zeta}_2 + k_1\dot{\tilde{\Delta}}) + 54.57\tilde{\zeta}_2 + \alpha_{2s}) \le \varepsilon_2 \end{aligned} \quad (24)$$

where $\varepsilon_1, \varepsilon_2$ are design parameters. The adaptation terms are selected to be

$$\tau_1 = 614.6 z_2 u \quad \tau_2 = 614.6 z_2\,. \quad (25)$$

For implementation proportional gains are used for the robust control terms α_{is}, and are lumped with the k_i gains. Control gains of $k_1 = 10$ and $k_2 = 50$ place the error system poles near the open-loop system poles to ensure reasonable settling times and control efforts. The adaptation gains are selected as $\gamma_1 = 2e-11$ and $\gamma_2 = 2e-4$, which provided a good balance between adaptation speed and noise sensitivity in simulation. The parameter estimates were limited to the ranges $0.75 \le \theta_1 \le 1.25$ and $-500 \le \theta_2 \le 500$ to correspond with the experimentally observed process variation.

A. Observer Design

The ADDF developed in [23] is applied directly to estimate the unmeasured states. The ADDF operates on systems of the form

$$\begin{aligned} x_{k+1} &= f_m\,(x_k, u_{x,k}) + w_{x,k} \\ y_k &= H x_k + w_{y,k} \end{aligned} \quad (26)$$

where $x_k \in R^n$ is the state vector restricted to the compact domain $D \subset R^n$, $y_k \in R^p$ is the output vector, $u_{x,k} \in R^m$ is the input vector, and the globally Lipschitz nonlinear plant model is $f_m\,(x_k, u_{x,k})$. $w_{x,k}$ and $w_{y,k}$ are independent, identically distributed Gaussian random variables with covariances Q_k and R_k.

The ADDF is applied to the FSW system model by using an Euler integration to discretize the continuous model. The observer state vector is defined to be $x_k = \zeta\,(t_k)$ with input $u_{x,k} = u\,(t_k)$. The state transition function can then be defined as $f_m = (Ax_k + B\theta_1 u_{x,k})\,t_s + x_k$, where t_s (s) is the discrete time step. The output is defined as $y_k = f^*_z\,(t_k)$ with $H = C$. The noise terms $w_{x,k}$ and $w_{y,k}$ are not known, nor are they required for implementation of the ADDF. However, the noise covariance terms Q_k and R_k must be specified. Since the true covariance values are unknown, the terms are used as tuning parameters that describe the error expected from the system model and measurement. Other parameters include $\hat{P}^u_0$, which relates to the confidence in the initial state estimate α, which scales the state estimate covariance increase at each time step β, which determines the amount of adaptation allowed, and ρ, which determines the weighting given to *a priori* covariance data. A complete explanation of the parameters is given in [23]. The parameter values selected for the experiments in this work are given in Table III. After specifying these tuning parameters the ADDF implementation is completely systematic.

TABLE III
ADDF PARAMETER VALUES

Parameter	Description	Value
$\hat{P}^u_0$	Initial state covariance estimate	$10I$
Q_k	Process noise covariance	$10^{-6}I$
R_k	Output noise covariance	10^{-6}
α	Tuning parameter	10
β	Tuning parameter	2
ρ	Tuning parameter	0.2

TABLE IV
AXIAL WELDING FORCE EXPERIMENTAL PROCESS CONDITION SETS

Exp. #	1–3	4–6	7–9
Exp. Cond. Set #	1	2	3
Spindle Speed (RPM)	2500	2000	2250
Plunge Depth (mm)	0.11	0.20	0.15
Des. Axial Force (N)	2000	2300	2300

VI. EXPERIMENTAL RESULTS

Experiments were conducted to verify the functionality of the ARC/ADDF approach. Each run consisted of plunging the tool into the material at 12 mm/min, then preheating the part by moving in the traverse direction for 3 mm at a rate of 6 mm/min. Control was then enabled and welding was performed until a total length of 90 mm had been traversed. To maintain consistency between experiments, subsequent welding was not performed until the workpiece temperature had returned to 30 °C or less. Three sets of process conditions within the modeled parameter range were tested (see Table IV). The expected axial force variation is above 25% of the desired value for each condition set. Three runs of each set were performed to verify repeatability.

Fig. 8 shows the measured and calculated (i.e., spindle power-based) axial force typical of each condition set. The commanded velocity results for each set are shown in Fig. 9. The estimated

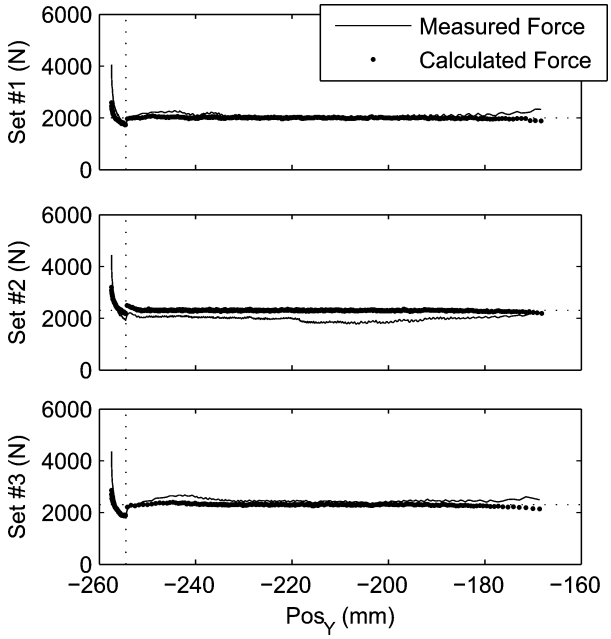

Fig. 8. Calculated and measured axial force for each experimental condition set. Horizontal dotted lines indicate desired force.

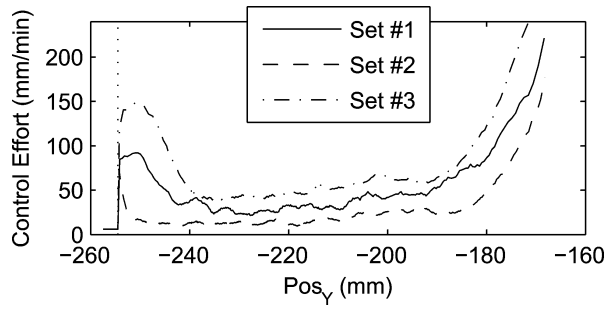

Fig. 9. Commanded velocity for each experimental condition set.

parameter values are shown in Fig. 10. Vertical dotted lines indicate the start of control. In the preheating section prior to the start of control the traverse rate is fixed at 6 mm/min, and the axial force decreases as the process approaches equilibrium after the tool is plunged into the work piece. In each case, the calculated axial force is maintained at or very near the desired force during the controlled portion of the weld. The average 1% settling time is 0.257 s. Fig. 10 shows that the adaptation mechanism responds correctly to significant disturbances. External disturbances of 250–500 N are estimated with θ_2, while θ_1 varies by up to 10%, which corresponds to a change in input of up to 230 N.

The only significant deviation from the desired force occurs at the end of the weld when the tool is approaching the end of the workpiece. This behavior can be attributed to significant heat buildup in the workpiece near the edges. As the tool approaches the workpiece edge heat generated by the tool can no longer be transferred away from the tool in all directions. The heat is instead reflected by the end of the workpiece, causing the material temperature near the tool to increase significantly. This heat buildup softens the material and reduces weld forces. The

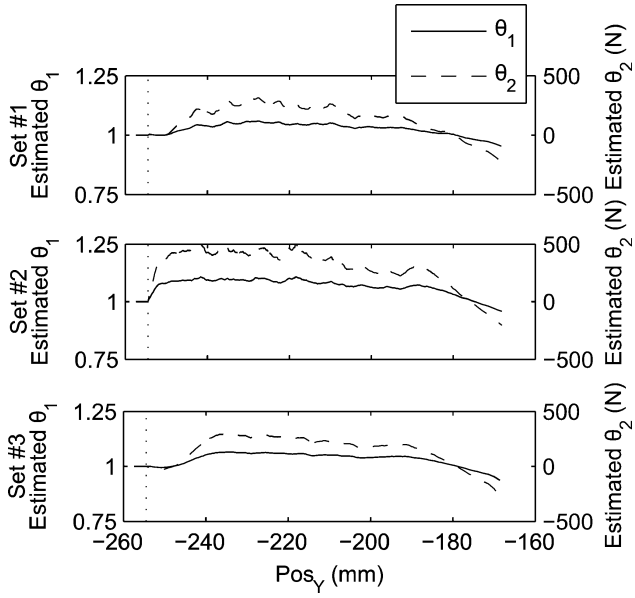

Fig. 10. Estimated values of unknown parameters for each experimental condition set.

controller responds by increasing traverse velocity to near the allowed maximum of 240 mm/min.

In each case, some discrepancy is observed between the calculated axial force derived from the spindle power and the actual axial force measured by the dynamometer. More interestingly, the slopes are not always in agreement. The discrepancy indicates that the method used to calculate axial force from spindle motor power (5) does not consider all the necessary variables. Similarities in the shape of the actual power measurement and the velocity profile hint that the force calculation could be improved by also considering the traverse velocity in (5).

These results demonstrate the effective control of FSW axial force by manipulating the traverse velocity. The combined ARC/ADDF approach is shown to perform well even in the presence of significant process variation and model error. Using the spindle motor power as a measure of axial force is also shown to be feasible, but may require further refinement if more accurate control is required.

VII. Conclusion

The FSW is a new and advantageous welding technique, but can produce welds of inconsistent quality when performed with constant process parameters. To improve weld consistency, axial force control was implemented in this paper. An observer-based nonlinear controller was constructed using the systematically applicable ARC and ADDF techniques. Experimental implementation shows that the control approach offers significant improvements to the weld force consistency in the presence of large model uncertainty and external disturbances. Comparisons between the actual force and the spindle power-based calculated force indicate that the modeled relationship could be improved.

References

[1] Z. Y. Ma, "Friction stir processing technology: A review," *Metallurgical*

Mater. Trans. A—Phys. Metallurgy Mater. Sci., vol. 39 A, pp. 642–658, Mar. 2008.
[2] G. E. Cook, R. Crawford, D. E. Clark, and A. M. Strauss, "Robotic friction stir welding," *Ind. Robot—Int. J.*, vol. 31, pp. 55–63, 2004.
[3] X. Zhao, P. Kalya, R. G. Landers, and K. Krishnamurthy, "Design and implementation of nonlinear force controllers for friction stir welding processes," *Trans. ASME, J. Manuf. Sci. Eng.*, vol. 130, pp. 061011-1–061011-10, Dec. 2008.
[4] T. Oakes and R. G. Landers, "Design and implementation of a general tracking controller for friction stir welding processes," in *Proc. Amer. Control Conf.*, St. Louis, MO, 2009, pp. 5576–5581.
[5] M. Soron and I. Kalaykov, "A robot prototype for friction stir welding," in *Proc. IEEE Conf. Robot., Autom. Mechatron.*, Bangkok, Thailand, 2006, pp. 1–6.
[6] K. Elangovan, V. Balasubramanian, and M. Valliappan, "Effect of tool pin profile and tool rotational speed on mechanical properties of Friction Stir Welded AA6061 aluminium alloy," *Mater. Manuf. Process.*, vol. 23, pp. 251–260, 2008.
[7] R. Nandan, T. DebRoy, and K. H. D. H. Bhadseshia, "Recent advances in friction-stir welding—Process, weldment structure and properties," *Progr. Mater. Sci.*, vol. 53, pp. 980–1023, 2008.
[8] C. I. Huang and L. C. Fu, "Adaptive approach to motion controller of linear induction motor with friction compensation," *IEEE/ASME Trans. Mechatronics*, vol. 12, no. 4, pp. 480–490, Aug. 2007.
[9] S. H. Hsu and L. C. Fu, "Adaptive decentralized control of robot manipulators driven by current-fed induction motors," *IEEE/ASME Trans. Mechatronics*, vol. 10, no. 4, pp. 465–468, Aug. 2005.
[10] S. Bashash and N. Jalili, "Robust adaptive control of coupled parallel piezo-flexural nanopositioning stages," *IEEE/ASME Trans. Mechatronics*, vol. 14, no. 1, pp. 11–20, Feb. 2009.
[11] X. Yue, D. M. Vilathgamuwa, and K. J. Tseng, "Robust adaptive control of a three-axis motion simulator with state observers," *IEEE/ASME Trans. Mechatronics*, vol. 10, no. 4, pp. 437–448, Aug. 2005.
[12] T. Nguyen, J. Leavitt, F. Jabbari, and J. E. Bobrow, "Accurate sliding-mode control of pneumatic systems using low-cost solenoid valves," *IEEE/ASME Trans. Mechatronics*, vol. 12, no. 2, pp. 216–219, Apr. 2007.
[13] B. Yao and M. Tomizuka, "Adaptive robust control of SISO nonlinear systems in a semi-strict feedback form," *Automatica*, vol. 33, pp. 893–900, 1997.
[14] M. Krstić and I. Kanellakopoulos, *Nonlinear and Adaptive Control Design*. New York: Wiley, 1995.
[15] B. Yao, "High performance adaptive robust control of nonlinear systems: A general framework and new schemes," in *Proc. 36th IEEE Conf. Decis. Control*, San Diego, CA, 1997, pp. 2489–2494.
[16] X. C. Zhu, G. L. Tho, B. Yao, and J. Cao, "Adaptive robust posture control of parallel manipulator driven by pneumatic muscles with redundancy," *IEEE/ASME Trans. Mechatronics*, vol. 13, no. 4, pp. 441–450, Aug. 2008.
[17] S. K. Spurgeon, "Sliding mode observers: A survey," *Int. J. Syst. Sci.*, vol. 39, pp. 751–764, 2008.
[18] J. Zhou, G. O. Kaasa, and O. M. Aarno, "Nonlinear adaptive observer control for a riser slugging system in unstable wells," in *Proc. 2008 Amer. Control Conf.*, 2008, vol. 1–12, pp. 2951–2956.
[19] B. Yao and L. Xu, "Observer-based adaptive robust control of a class of nonlinear systems with dynamic uncertainties," *Int. J. Robust Nonlinear Control*, vol. 11, pp. 335–356, 2001.
[20] M. Boutayeb and D. Aubry, "A strong tracking extended Kalman observer for nonlinear discrete-time systems," *IEEE Trans. Automat. Control*, vol. 44, no. 8, pp. 1550–1556, Aug. 1999.
[21] S. J. Julier and J. K. Uhlmann, "Unscented filtering and nonlinear estimation," *Proc. IEEE*, vol. 92, no. 3, pp. 401–422, Mar. 2004.
[22] M. Norgaard, N. K. Poulsen, and O. Ravn, "New developments in state estimation for nonlinear systems," *Automatica*, vol. 36, pp. 1627–1638, 2000.
[23] N. Subrahmanya and Y. C. Shin, "Adaptive divided difference filtering for simultaneous state and parameter estimation," *Automatica*, vol. 45, pp. 1686–1693, Jul. 2009.
[24] S. J. Rober and Y. C. Shin, "Modeling and control of CNC machines using a PC-based open-architecture controller," *Mechatronics*, vol. 5, pp. 401–420, 1995.
[25] C. Y. Xu and Y. C. Shin, "Control of cutting force for creep-feed grinding processes using a multi-level fuzzy controller," *Trans. ASME, J. Dyn. Syst., Meas., Control*, vol. 129, pp. 480–492, 2007.
[26] O. Frigaard, O. Grong, and O. T. Midling, "A process model for friction stir welding of age hardening aluminum alloys," *Metallurgical Mater. Trans. A—Phys. Metallurgy Mater. Sci.*, vol. 32, pp. 1189–1200, 2001.
[27] A. Fathi, A. Khajepour, M. Durali, and E. Toyserkani, "Geometry control of the deposited layer in a nonplanar laser cladding process using a variable structure controller," *Trans. ASME, J. Manuf. Sci. Eng.*, vol. 130, pp. 031003-1–031003-11, 2008.
[28] X. Zhao, P. Kalya, R. G. Landers, and K. Krishnamurthy, "Empirical dynamic modeling of friction stir welding processes," *Trans. ASME, J. Manuf. Sci. Eng.*, vol. 131, no. 2, pp. 021001-1–021001-9, 2009.

Tyler A. Davis received the M.S. degree from Brigham Young University, Provo, UT, in 2004. He is currently working toward the Ph.D. degree at Purdue University, West Lafayette, IN.

His current research interests include dynamics and control, machine vision, and mechatronics.

Yung C. Shin received the Ph.D. degree in mechanical engineering from the University of Wisconsin, Madison, in 1984.

From 1984 to 1988, he was a Senior Project Engineer at the GM Technical Center. From 1988 to 1990, he was with the faculty of Pennsylvania State University. In 1990, he joined Purdue University, West Lafayette, IN, where he is currently a Professor of mechanical engineering. He is the author or coauthor of more than 250 papers published in archived journals and refereed conference proceedings, is the author of chapters in several engineering handbooks and is a coeditor of two books. He also is a coauthor of *Intelligent Systems: Modeling, Optimization and Control* (CRC Press, 2008). He has organized or coorganized many conferences and symposia in his areas of research including the first and second *Artificial Neural Networks in Engineering Conference* and *Symposium on Neural Networks in Manufacturing and Robotics* and *Symposium on Intelligent Design and Manufacturing* at the American Society of Mechanical Engineers International Mechanical Engineering Congress and Exposition. His research interests include intelligent and adaptive control, process monitoring and diagnostics, laser processing of materials, high-speed machining, process modeling, and simulation.

Bin Yao (S'92–M'96) received the B.Eng. degree in applied mechanics from Beijing University of Aeronautics and Astronautics, Beijing, China, in 1987, the M.Eng. degree in electrical engineering from Nanyang Technological University of Singapore, Singapore, in 1992, and the Ph.D. degree in mechanical engineering from the University of California at Berkeley, in 1996.

Since 1996, he has been with the School of Mechanical Engineering, Purdue University, West Lafayette, IN, where he was promoted to an Associate Professor in 2002 and a Professor in 2007. He was honored as a Kuang-piu Professor in 2005 and a Chang Jiang Chair Professorship in 2010 at Zhejiang University in China as well.

Prof. Yao received a Faculty Early Career Development (CAREER) Award from the National Science Foundation (NSF) in 1998 and a Joint Research Fund for Outstanding Overseas Chinese Young Scholars from the National NSF of China in 2005. He was also the recipient of the O. Hugo Schuck Best Paper (Theory) Award from the American Automatic Control Council in 2004 and the Outstanding Young Investigator Award of the ASME Dynamic Systems and Control Division in 2007.